International Journal of Solids and Structures 46 (2009) 3480–3491

Contents lists available at ScienceDirect

International Journal of Solids and Structures

journal homepage: www.elsevier.com/locate/ijsolstr

New experimental and numerical techniques to study the arrest and the restart of a crack under impact in transparent materials

David Grégoire *, Hubert Maigre, Alain Combescure

Université de Lyon, CNRS, INSA-Lyon, LaMCoS UMR5259, F-69621, France

ARTICLE INFO

Article history:
Received 4 February 2009
Received in revised form 11 May 2009
Available online 7 June 2009

Keywords:
Dynamic brittle fracture
Crack arrest
Crack restart
X-FEM
Experiments
Kolsky bars (SHPB)
PMMA
Crack location

ABSTRACT

The determination of relevant constitutive crack propagation laws under dynamic loading is a rather challenging exercise. In dynamic impact cases, the variations of propagation parameters and the extractions of crack positions are difficult tasks. This paper focuses on a methodology for assessing dynamic crack propagation laws under impact loading for transparent materials. Dynamic brittle fracture experiments are performed on polymethyl methacrylate (PMMA) in which several crack arrest phases occur. Then, these experiments are numerically reproduced by using the eXtended Finite Element Method (X-FEM) in order to validate the algorithms and the criteria assumed.

1. Introduction

The risks due to crack propagation under dynamic loading are still difficult to estimate. Unlike quasi-static cases, where the loading and crack position can be easily established, in dynamic impact cases, loading conditions, propagation parameter variations and exact crack positions are difficult to control. The determination of relevant constitutive crack propagation laws from dynamic crack propagation experiments is thus a challenging operation. Consequently, the first step for assessing dynamic crack propagation laws is the development of numerical simulation tools.

Since the 70s, a large effort has been put into the development of numerical tools dedicated to the crack growth simulation, especially for the fatigue phenomenon. The main difficulty consists in following the crack geometry over time. During the last years, alternative methods based on the partition of unity (Babuska and Melenk, 1997) allowed an implicit description of the evolving discontinuities. Thereby, the eXtended Finite Element Method (X-FEM) seems specially adapted to the simulation of the dynamic propagation under impact loading, since the crack paths are *a priori* unknown. If the method had been initially developed in quasi-statics (Belytschko and Black, 1999; Moës et al., 1999), the advantages of the X-FEM for the numerical simulation of dynamic fracture were discussed in many papers. It has been used to study the crack propagation in 2D (Prabel, 2007; Menouillard, 2007), in 3D (Duarte et al., 2001; Moës and Belytschko, 2002; Gravouil et al., 2002), with contact (Dolbow et al., 2001) or with cohesive zones (Moës and Belytschko, 2002). The numerical algorithms developed in this paper are based on the previous works of Réthoré et al. (2004, 2005a,b), Grégoire et al. (2007) and Combescure et al. (2008).

If some numerical tools are now able to represent dynamic crack growth, these numerical results have to be compared with experimental results to ensure that the numerical laws introduced are physically consistent.

Although many experiments have already been carried out, obtaining experimental results in dynamic crack propagation cases under impact loading is still difficult. The accurate measurement of the velocity of a crack under highly transient conditions is problematic. Strain gages (Owen et al., 1998; Maigre and Rittel, 1993; Rittel and Maigre, 1996), thin metal layer evaporated onto one specimen face (Fineberg et al., 1991; Stalder et al., 1983), common electrical or optical techniques are traditionally used with contrasting results. Precious experimental results have already been obtained and interesting phenomena have been highlighted, but these results are not as precise as required to validate the new models and the new numerical tools which are now developed.

In a previous work (Grégoire et al., 2007), crack tip position histories have been determined by standard optical tools. The test rig was a split Hopkinson pressure bar (SHPB) and the specimen geometry was chosen in order to provide direct conversion

* Corresponding author. Tel.: +1 847 467 76 73; fax: +1 847 491 32 34.
E-mail address: david.gregoire@ens-cachan.org (D. Grégoire).
URL: http://lamcos.insa-lyon.fr (A. Combescure).

0020-7683/$ - see front matter © 2009 Elsevier Ltd. All rights reserved.
doi:10.1016/j.ijsolstr.2009.06.003

between impacting compressive waves and tensile waves in the vicinity of a machined notch. Since the material used (PMMA) was transparent, four high-speed cameras, connected through a delay line (time resolution: 1 μs), were used to provide pictures of the propagating crack tip. During each test, each camera provides one picture. Hence, four pictures are obtained at four different instants during each test. By checking that the results were highly reproducible, five experimental tests were carried out by modifying the shooting sequence through the delay line. All crack tip positions were collected to obtain the crack tip position history. Three different phases were observed: two propagation phases separated by a crack arrest phase. These three phases occurred during a highly transient phase and these conditions provided a challenging test of the reliability of the numerical simulations. Using an X-FEM, numerical simulations were performed and both the crack path and the crack position histories fitted the experimental results.

This kind of comparison allowed the validation of a dynamic crack growth criterion but only in a unique case of loading. The next step in the dynamic crack propagation laws assessment should be to show how the dynamic crack growth criterion depends on the loading conditions. However, with standard optical tools such as cameras, the previous process leads to a large number of experiments for obtaining different crack tip position histories corresponding to different loading rate. Moreover, the loading rate influence on the transient propagation phases as arrest and restart cannot be represented accurately if several experiments are needed to obtain a crack tip position history. Therefore new experimental methods are required to assess relevant constitutive crack propagation laws from experiment.

This paper focuses on a methodology for assessing dynamic crack propagation laws under impact loading for transparent materials. Firstly, a new technique is presented for the accurate crack tip position histories measurement during dynamic crack propagation experiments under impact in transparent materials. Secondly, these experiments are reproduced by using an X-FEM numerical tool in order to validate the dynamic crack propagation laws assumed.

2. Crack tip location using an optical displacement sensors

2.1. Description of the test rig and the specimen

The test rig is a SHPB test developed by Kolsky (1949) and primarily used for the measurement of a material dynamic behavior. It is schematized in Fig. 1. The test specimen is made of polymethyl methacrylate (PMMA), a transparent brittle material. The mechanical properties of nylon and PMMA are quite similar. Therefore, the chosen bars are made of nylon in order to guarantee both a good wave transmission on their interfaces with the specimen and an elastic strain gage response. Details on the experimental setup are presented in Grégoire et al. (2007).

There is no standard for dynamic fracture tests. Therefore a simple, but distinctive, geometry designed is chosen to obtain transient propagation phases as crack arrest and restart. The specimen is shown in Fig. 1 and its dimensions are given in Fig. 2.

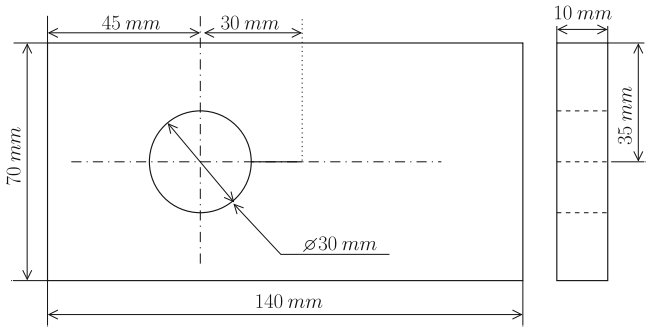

Fig. 2. Specimen geometry under pure mode I loading condition.

The compressive waves must be converted into tensile waves, in order to obtain fracture opening modes at the crack tip. Therefore, a rectangular specimen with a circular hole is used to provide the direct wave conversion without producing any friction at the specimen–bars interfaces. In addition, crack arrest is provided by a circular hole as suggested by Karimzada and Maigre (2000) and studied by Grégoire et al. (2007). An initial notch is machined at the border of the hole in order to initiate the crack. The initial notch is not represented in Fig. 1 because several choices are possible. Fracture occurs in pure mode I when the initial notch is machined on the specimen symmetry axis. Fracture occurs in mixed-mode when the initial notch is moving from the specimen symmetry axis. In this study, the initial notch is machined on the specimen symmetry axis as shown in Fig. 2 (a fracture initiation in mixed-mode is presented in Grégoire et al. (2007)). Fig. 3 presents a typical microscopic view of the notch tip. Since the initial notch is machined with a model saw, the notch tip has a rectangular shape.

2.2. Measurement

The use of SHPB is attractive in our case because it provides both an accurate measurement of the applied loading and the global response of the test specimen during the transient experiment, thus enabling good control of the quality of the experimental tests. Reliable experimental data are necessary to ensure that the simulations are physically meaningful. This is one of the keys to success in comparing numerical simulations with experiments.

Fig. 4 shows a sketch of the test rig. One can identify:

- the striker bar, input bar and output bar and the specimen between the bars;
- two strain gages connected to their amplifiers;
- one optical displacement sensor (Zimmer);
- one standard light;
- one data acquisition adapter (four channels, 1 MHz);
- one optical sensor connected to an oscilloscope;
- two computers.

Since PMMA is transparent, an optical displacement sensor is used. A Zimmer extensometer converts the movement of a black and white target into an analog signal (±5 V) proportional to the

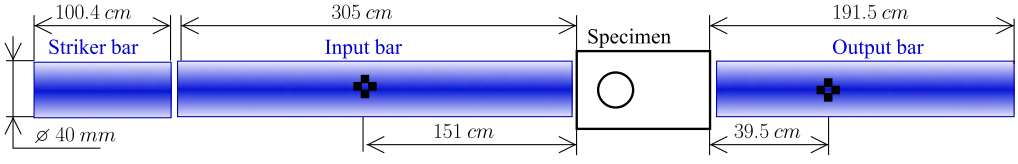

Fig. 1. Characteristics of the split Hopkinson pressure bar.

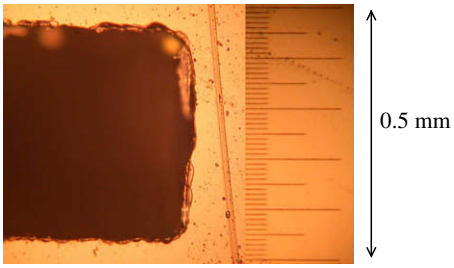

Fig. 3. Microscopic view of the notch tip (test 1 – striker velocity: 9.5 m/s).

displacement of the black and white contrasted border. The measurement range is determined by the adaptive lens. The Zimmer extensometer was primarily used to measure the macroscopic displacements of a body by sticking on it a black and white target (Fig. 5).

Since the light reflects on the crack path and transmits through the uncracked part of the specimen (Fig. 6), an analogical signal proportional to the crack tip position is obtained. The resolution, the working distance, the uncertainty and the width of the measure as well as the maximum tracking velocity depend on the measurement range linked to the choice of lens. The characteristics of the optical displacement sensor are collected in Table 1.

The loading is adjusted via several experiment parameters: the velocity, the length and the shape of the striker bar enabled to control the amplitude, the duration and the shape of the loading. Two different experiments are performed with the specimen geometry corresponding to pure mode I initiation. The experimental condi-

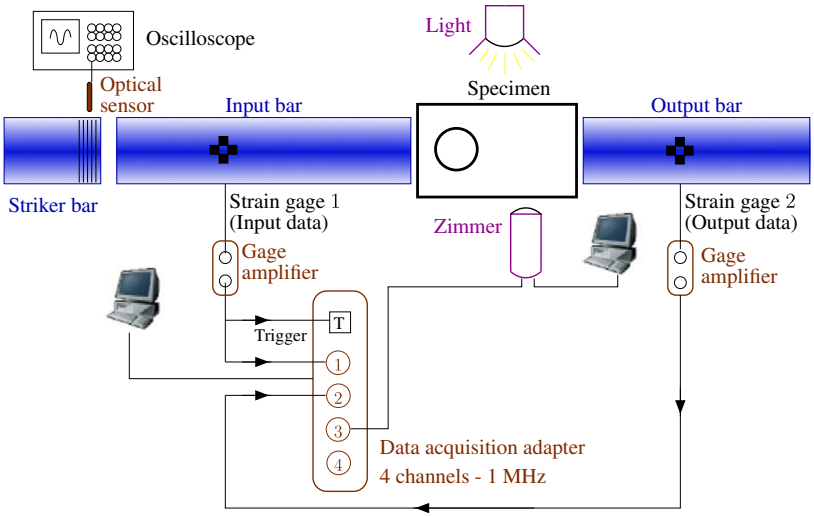

Fig. 4. Experimental test rig (One Zimmer).

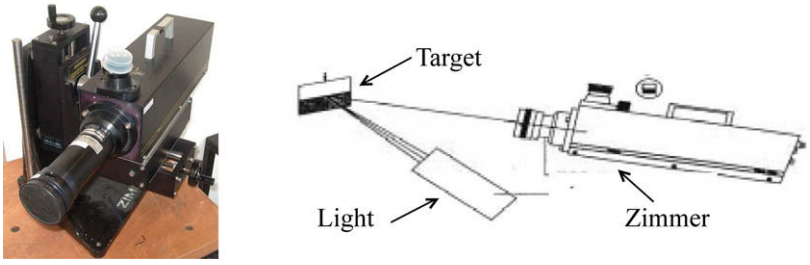

Fig. 5. Zimmer usually used to measure macroscopic displacements.

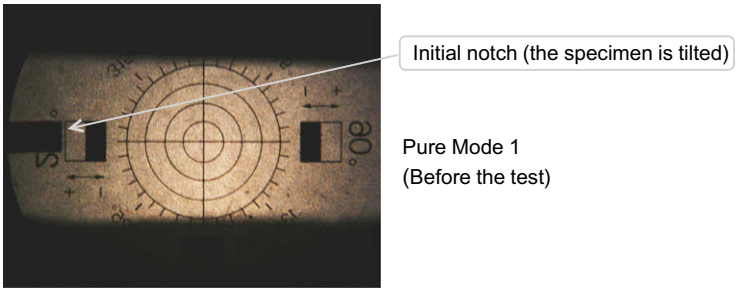

Fig. 6. Zimmer used for dynamic crack tip location.

Table 1
Characteristics of the optical displacement sensors.

Measurement range	20 mm
Working distance	41.1 mm
Measurement width	1 mm
Resolution	0.002 mm
Uncertainty	±0.04 mm
Maximum tracking velocity	1670 m/s

Table 2
Experimental conditions.

Experiment	Initiation	Striker length (m)	Striker velocity (m/s)
Test 1	Mode I	1.004	9.5
Test 2	Mode I	1.004	7.4

Uncertainty: 0.08 m/s.

tions are described in Table 2. The striker velocity is measured by an optical sensor linked to an oscilloscope (Fig 4).

To limit wave superposition, the gages are generally located at the middle of the bars (Fig. 1). Consequently, the waves have to be shifted to the specimen–bar interfaces to obtain forces and velocities at the specimen faces. Waves dispersion and attenuation due to the viscous behavior of nylon and geometry effects are taken into account in the shifting as in Zhao and Gary (1995) in order to obtain more accurate measurements. The same process is performed for each experimental test. For instance, raw data corresponding to the test 1 are shown in Fig. 7 and the corresponding input and output velocities at the specimen–bar interfaces are shown in Fig. 8. The time when compressive waves reach the left-hand face of the specimen is chosen as the reference time.

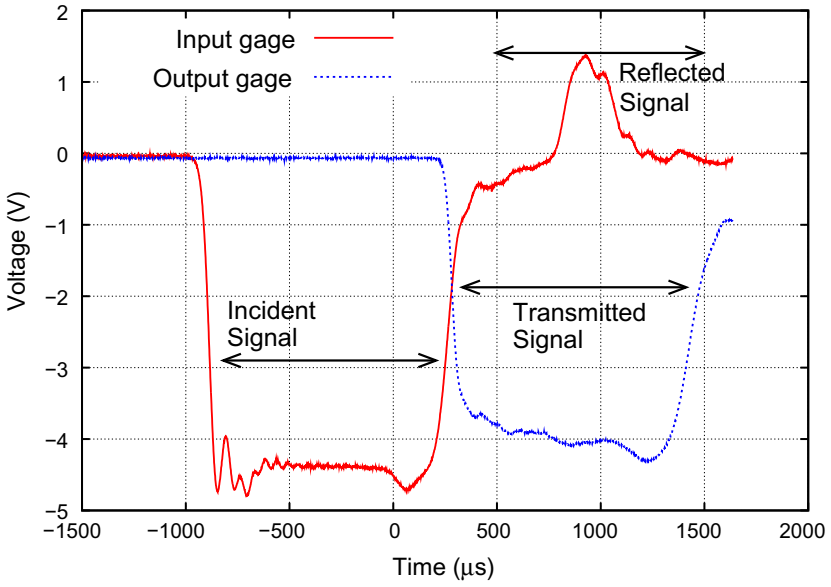

Fig. 7. Unprocessed gage signals (test 1 – striker velocity: 9.5 m/s).

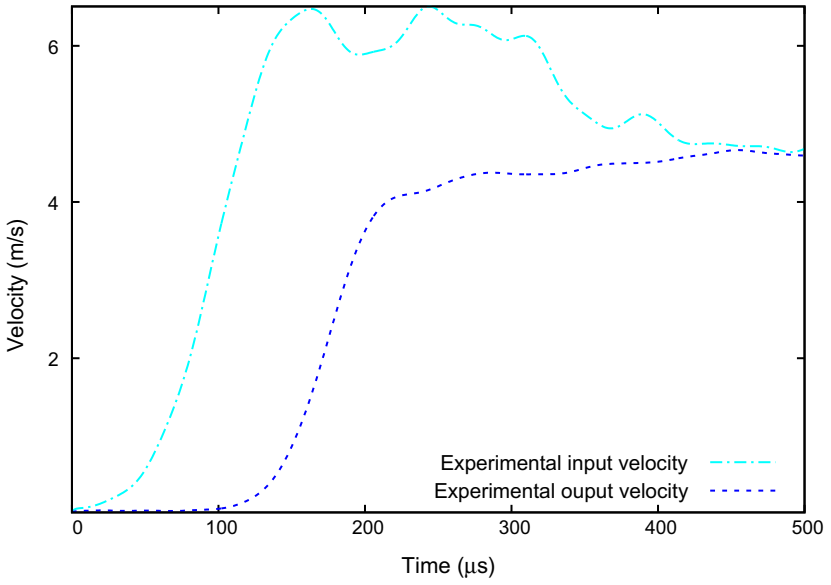

Fig. 8. Velocities at the specimen–bar interfaces (test 1 – striker velocity: 9.5 m/s).

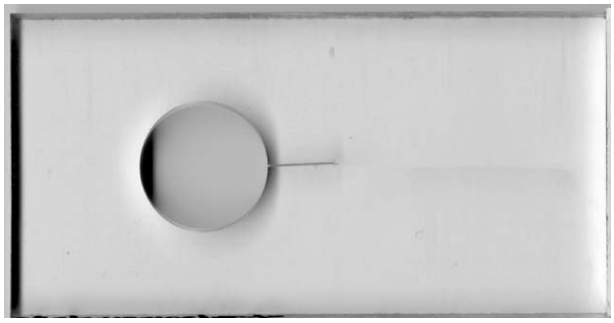

Fig. 9. *Postmortem* view of the crack path (test 1 – striker velocity: 9.5 m/s).

2.3. Experimental results

This section presents the experimental results obtained with the specimen geometry under pure mode I loading (see Fig. 2). Two experiments have been performed with different impact velocities (test 1 and test 2 in Table 2).

During these experiments, a Zimmer extensometer (see Table 1) has been used to obtain the crack tip position history. Since the measurement range is 20 mm, the entire crack propagation history cannot be obtained. The time when the optical displacement sensor starts producing a signal is chosen as the reference time. Furthermore, the X-coordinate reference corresponds to the left-hand face of the specimen (after the initiation, the crack grows from $x = 75$ mm).

The extensometer measured the absolute displacement of the crack tip, including the solid body motion of the specimen. Therefore, the crack growth is obtained by subtracting the second to the former. The solid body motion of the specimen is measured from the Zimmer extensometer signal during the crack arrest phase and it is assumed to be constant during all the crack propagation. Hence this value is used in the subtraction process. Moreover, the extensometer signal is shifted in order to adjust the crack arrest with the position measured on the crack path *postmortem* view.

2.3.1. Test 1 (striker velocity: 9.5 m/s)

The raw data corresponding to the test 1 are shown in Fig. 7 and the corresponding input and output velocities at the specimen–bar interfaces are shown in Fig. 8. The time when compressive waves reach the left-hand face of the specimen is chosen as the reference time. Fig. 3 presents a microscopic view of the notch tip before the dynamic fracture test (notch tip radius ≈0.22 mm) and Fig. 9 shows a *postmortem* picture of the specimen for the test 1.

Fig. 10 shows the propagating crack tip position history for the test 1 and three different propagation phases are observed:

- Firstly, the crack grows at constant velocity ($V \approx 170$ m/s).
- Secondly, the crack stops during approximately 65 μs.
- Finally, the crack restarts at constant velocity ($V \approx 180$ m/s).

A large jump in the crack propagation velocity during the arrest and the restart of the crack is noticed in Fig. 10. Indeed, the crack propagation velocity decreases suddenly from $V \approx 170$ m/s to $V = 0$ m/s during the crack arrest phase. In the same way, the crack speeds up suddenly from $V = 0$ m/s to $V \approx 180$ m/s during the restart phase. Thereby, this method based on optical displacement sensor measurement provides an accurate crack tip location, even during the highly transient propagation phases such as arrest and restart. Therefore, it is now possible to study the influence of the loading rate on these transient propagation phases.

2.3.2. Test 2 (striker velocity: 7.4 m/s)

Since the initiation strongly depends on the initial notch shape, the experimental test 2 was performed in two stages. First, a short crack propagation (3.5 mm) is obtained by impacting the specimen at a low velocity. The specimen is then submitted to a second stronger impact. The notch tip shape after the first arrest is therefore similar to the crack tip shape during the transient propagation. Fig. 11 presents a microscopic view of the notch tip after the first arrest and before the second stronger impact (notch tip radius ≈1 μm). This technique can be linked to the fatigue crack growth initiation for metallic materials. The input and output velocities at the specimen–bar interfaces are shown in Fig. 12, and Fig. 13 shows a *postmortem* picture of the specimen for the test 2.

Fig. 14 shows the propagating crack tip position history for the test 2 where the striker velocity was lower than the striker velocity of the test 1. Four crack arrests are now observed. After the initiation, the cracks grows during 54 μs at a constant velocity of ($V \approx 150$ m/s) and then stops during 103 μs. Afterwards, there are three short propagating phases separated by crack arrests before the final arrest. Strong jumps in the crack propagation velocity are still noticed in Fig. 14, in spite of the presence of several crack

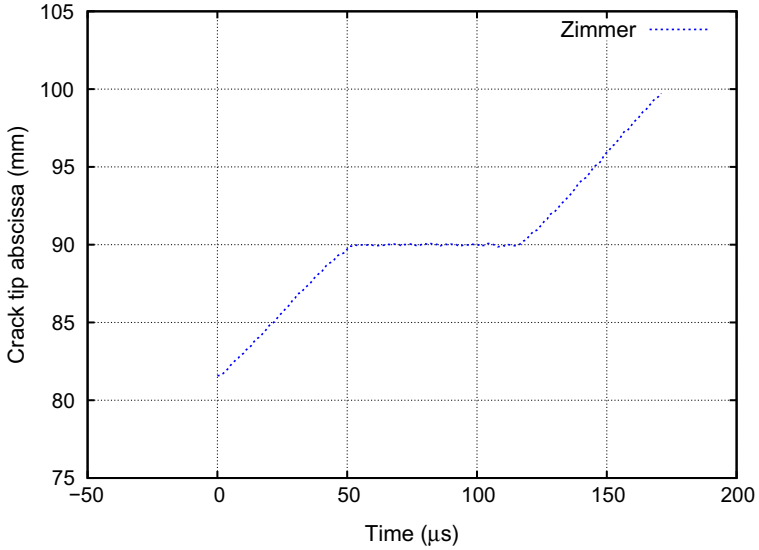

Fig. 10. Crack tip position history (test 1 – striker velocity: 9.5 m/s).

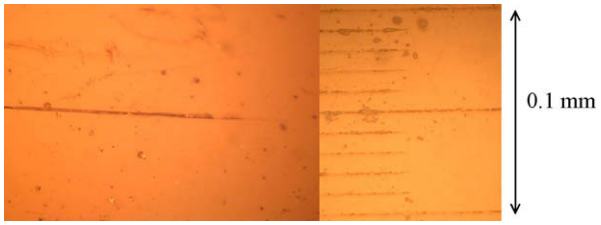

Fig. 11. Microscopic view of the notch tip (test 2 – striker velocity: 7.4 m/s).

arrest and restart phases.This phenomenon is comparable to the stick-slip phenomenon. The crack never slows down but only stops or propagates. Therefore, a minimum crack tip velocity seems needed when the crack propagates. Below this threshold, the crack just does not propagate. It is a unique phenomenon due to the dynamic crack propagation, really different from the phenomenon noticed during stable steady-state propagation where the crack tip velocity can be adjusted through the loading rate.

This kind of experiment provides a challenging test of the reliability of the dynamic crack propagation numerical tools as well as a mean for assessing new constitutive crack propagation laws. It is certain that this kind of result cannot be obtained with standard optical tools such as cameras where several experiments are needed to collect the crack tip position history. The crack behavior during the high transient propagation phases such as crack arrest and crack restart can be studied accurately only if the whole crack tip position history is obtained during a single test. It is the main advantage of the proposed method based on optical displacement sensor measurement. Finally, one may conclude that a new experimental technique has been developed to determine very accurate dynamic crack tip location under impact loading in transparent materials.

3. Numerical simulations

3.1. Spacial discretization

The X-FEM is chosen for the simulations because the cracks are not described explicitly by the mesh. Furthermore, the implicit description of a crack geometry is compatible with any crack path, even if this path is *a priori* unknown.

In order to capture the discontinuity and singularity of the strain field at the crack tip, we use an enrichment to the classical

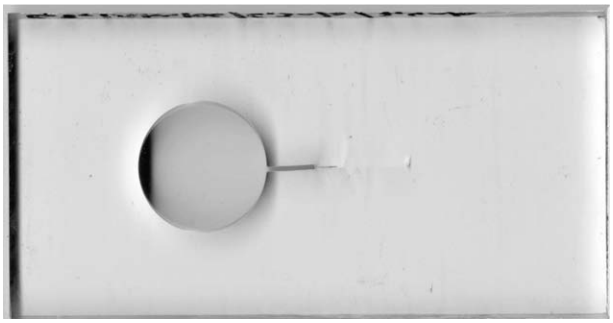

Fig. 13. *Postmortem* view of the crack path (test 2 – striker velocity: 7.4 m/s).

finite element approximation defined through the partition of unity method developed by Babuska and Melenk (1997). This method was first developed for quasi-static analysis in Belytschko and Black (1999) and Moës et al. (1999). Here, the method is used for dynamic crack propagation as in Grégoire et al. (2007) in the light of Réthoré et al. (2005b). More details can be found in these papers.

The crack is represented by a set of straight segments. For the description of the crack to be independent of the mesh, discontinuous enrichments are added to the set of the nodes which have their support entirely cut by the crack, while the set of the nodes which contain the crack tip in their support is enriched by a singular set of functions. When the crack propagates this set is modified as follows: all ancient enrichments are kept. New enrichments corresponding to the new position of the crack are simply added to the old set.

The approximation of the displacement fields is then written as:

$$\widetilde{U}(t) = \sum_{i\in\mathcal{N}} N_i(x)u_i(t) + \sum_{i\in\mathcal{N}^e_{\text{cut}}(t)} N_i(x)\mathscr{H}(x)a^e_i(t) + \sum_{i\in\mathcal{N}^e_{\text{tip}}(t)} \times \sum_{j\in[\![1,4]\!]} N_i(x)B^e_j b^e_{ij}(t) \tag{1}$$

where, at time t, $N^e_{\text{cut}}(t)$ is the set of the nodes which have had their support entirely cut by the crack, $a^e_i(t)$ are the nodal degrees of freedom corresponding to the step function $\mathscr{H}$, $N^e_{\text{tip}}(t)$ is the set of the nodes which have contained the crack tip in their support, $b^e_{ij}(t)$ are the nodal degrees of freedom corresponding to the functions B^e_j which span the near-tip asymptotic fields.

According to Moës et al. (1999):

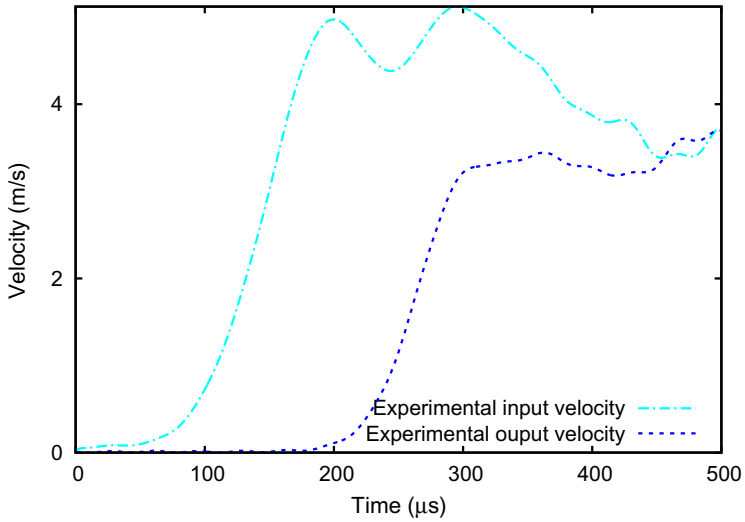

Fig. 12. Velocities at the specimen–bar interfaces (test 2 – striker velocity: 7.4 m/s).

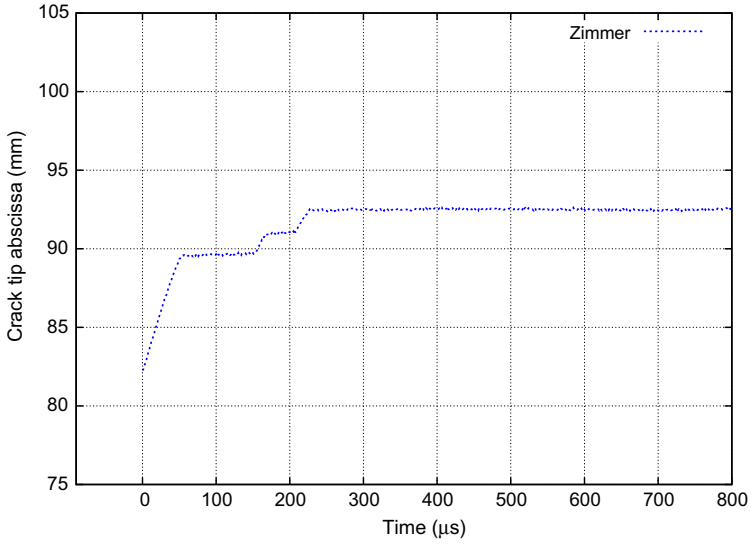

Fig. 14. Crack tip position history (test 2 – striker velocity: 7.4 m/s).

$$\mathscr{H}(x) = \begin{cases} +1 & \text{if } x \text{ is above the crack} \\ -1 & \text{if } x \text{ is below the crack} \end{cases} \tag{2}$$

$$\left\{B_j^e(r,\theta)\right\}_{j\in[\![1,4]\!]} = \left\{\sqrt{r}\cos\frac{\theta}{2}, \sqrt{r}\cos\frac{\theta}{2}\sin\theta, \sqrt{r}\sin\frac{\theta}{2}, \sqrt{r}\sin\frac{\theta}{2}\sin\theta\right\} \tag{3}$$

where (r,θ) are the local polar coordinates of the crack tip.

3.2. Temporal discretization and boundary conditions

The displacements, velocities and accelerations are discretized through Eq. (1) and the mass and stiffness matrices are calculated using ad hoc integration techniques for X-FEM elements (Moës et al., 1999). The discrete equation at time t_n is:

$$M_n\ddot{U}_n + K_nU_n = F_n \tag{4}$$

where M_n and K_n are the mass and stiffness matrices at time t_n and F_n is the vector of external forces at time t_n.

It was proved by Réthoré et al. (2005b) that if all singular enrichments are kept and the new enrichments are initialized to zero, using a Newmark scheme, stability and exact conservation of the discretized energy are guaranteed. The proof of the discretized energy conservation can be found in Combescure et al. (2008). The discretized dynamic equations (4) and (7) are chosen such that they can be integrated numerically using Newmark's implicit mean acceleration scheme (see Eq. (8)).

The numerical simulations are carried out using the input velocity collected from the experiments (Fig. 8) as a boundary condition at the input bar interface and an impedance condition is used to model the contact between the output bar and the specimen (this choice is discussed in Grégoire et al. (2007)). At each interface node of the output bar interface, the stress and velocity are assumed to be related by:

$$\begin{cases} \sigma\cdot n = -z\,(v\cdot n)\,n \text{ on } \partial\Omega_{\text{Int}} \\ z = \rho^{\text{bar}}\,c_L^{\text{bar}} \end{cases} \tag{5}$$

where σ and v are the stress and velocity on the specimen face, z is the impedance, $\partial\Omega_{\text{Int}}$ the interface and n a normal vector, ρ^{bar} and c_L^{bar} are the density and the velocity of 1D elastic waves in the bar.

Then, the impedance matrix is calculated by integrating condition (5) at the interface:

$$(Z)_{ij} = \int_{\partial\Omega_{\text{Int}}} z\,((N_i.n)\,n)\cdot N_j\,dl \tag{6}$$

where Z is the impedance matrix, N_i and N_j are the shape functions of the displacement field (Eq. (1)).

Hence, the discrete form of Eq. (4) becomes:

$$M_n\ddot{U}_n + K_nU_n = F_n - Z_n\dot{U}_n \tag{7}$$

where M_n, K_n and Z_n are the mass, stiffness and impedance matrices at time t_n and F_n is the vector of external forces at time t_n.

In the framework of the implicit mean acceleration scheme (Newmark, 1959), the use of Taylor series leads to an one time step displacement scheme (Eq. (8)).

Knowing $\{U_n,\dot{U}_n,\ddot{U}_n,F_{n+1}\}$, find $\{U_{n+1},\dot{U}_{n+1},\ddot{U}_{n+1}\}$ such as:

$$\begin{aligned} &\left[\frac{M}{\beta\Delta t^2}+K+\frac{\gamma Z}{\beta\Delta t}\right]U_{n+1} = F_{n+1}+\left[\frac{M}{\beta\Delta t^2}+\frac{\gamma Z}{\beta\Delta t}\right]U_n^p - Z\dot{U}_n^p \\ &\times\begin{cases}\dot{U}_{n+1}=\dot{U}_n^p+\frac{\gamma}{\beta\Delta t}(U_{n+1}-U_n^p)\\ \ddot{U}_{n+1}=\frac{1}{\beta\Delta t^2}(U_{n+1}-U_n^p)\end{cases}\quad\text{with} \\ &\times\begin{cases}U_n^p=U_n+\Delta t\dot{U}_n+\left(\frac{1}{2}-\beta\right)\Delta t^2\ddot{U}_n\\ \dot{U}_n^p=\dot{U}_n+(1-\gamma)\Delta t\ddot{U}_n\end{cases} \end{aligned} \tag{8}$$

3.3. Crack propagation laws

The crack propagation laws are chosen according to the global macroscopic concept of stress intensity factor (Irwin, 1957) extended to elastodynamics within the framework of Bui (1978) and Freund (1990). Indeed, the stress intensity factors in modes I and II are chosen to describe the fracture since the PMMA has a brittle fracture behavior under dynamic loading. In the vicinity of the crack tip, the dynamic stress intensity factors in mode I and mode II are given (see Freund (1990) for details) by:

$$K_{\text{I}}^{\text{dyn}} = \lim_{r\to 0}\sqrt{2\pi r}\,\sigma_{22}(\theta=0) \quad\text{and}\quad K_{\text{II}}^{\text{dyn}} = \lim_{r\to 0}\sqrt{2\pi r}\,\sigma_{12}(\theta=0) \tag{9}$$

where (r,θ) are the local coordinates of the crack tip, $(K_{\text{I}}^{\text{dyn}},K_{\text{II}}^{\text{dyn}})$ are the dynamic stress intensity factors in modes I and II.

Since the direct identification from the singular enrichment functions is not accurate, a domain-independent integral is used to calculate the dynamic stress intensity factors $(K_{\mathrm{I}}^{\mathrm{dyn}}, K_{\mathrm{II}}^{\mathrm{dyn}})$ as developed by Réthoré et al. (2005b). In a dynamic brittle fracture framework, the fracture is assumed to be locally due to the tensile stresses and the fracture phenomenon is assumed to be governed by the intensity of the hoop stress near the crack tip (criterion developed by Erdogan and Sih (1963) and extended in dynamics by Maigre and Rittel (1993)). Therefore, the intensity of the loading near the crack tip K^* and the preferential propagation direction θ^* are calculating using Eqs. (10) and (11) (see Grégoire et al. (2007) for details). The notation are chosen in agreement with Kanninen and Popelar (1985) and Ravi-Chandar (2004)

$$\theta^* = 2\arctan\left(\frac{1}{4}\left[\frac{K_{\mathrm{I}}^{\mathrm{dyn}}}{K_{\mathrm{II}}^{\mathrm{dyn}}} - \mathrm{sign}\left(K_{\mathrm{II}}^{\mathrm{dyn}}\right)\sqrt{8+\left(\frac{K_{\mathrm{I}}^{\mathrm{dyn}}}{K_{\mathrm{II}}^{\mathrm{dyn}}}\right)^2}\right]\right) \tag{10}$$

$$K^* = \cos^3\frac{\theta^*}{2}\left|K_{\mathrm{I}}^{\mathrm{dyn}}\right| - \frac{3}{2}\cos\frac{\theta^*}{2}\sin\theta^* K_{\mathrm{II}}^{\mathrm{dyn}} \tag{11}$$

where $|K_{\mathrm{I}}^{\mathrm{dyn}}|$, the positive part of $K_{\mathrm{I}}^{\mathrm{dyn}}$, avoids any closure effect.

No propagation initiates as long as the maximum hoop stress intensity factor remains less than a critical value, the dynamic crack initiation toughness, K_{1d}. As soon as this threshold is reached, the direction of the maximum hoop stress defines the critical direction θ_c of the incipient propagation (Maigre and Rittel, 1993). The crack initiation criterion is:

$$\begin{aligned} &K^* < K_{1d} \quad \text{(no initiation)}\\ &K^* = K_{1d}, \quad \theta^* = \theta_c \quad \text{(initiation)} \end{aligned} \tag{12}$$

The dynamic crack initiation toughness is a material property which must be evaluated from experiments and which generally depends on the temperature and the loading rate $K_{1d}(\dot{\sigma}, T)$.

Following crack initiation, different criteria must be determined in order to take the crack growth process into account. During the dynamic growth of a crack, the instantaneous maximum hoop stress intensity factor stays equal to the dynamic crack growth toughness $K_{1D}(\dot{a}, T)$, which depends on the crack tip velocity $\dot{a}$ and the temperature. Then, the crack grows as long as K^* stays above another material property, the dynamic crack arrest toughness, which also depends on the temperature and the loading rate $K_{1a}(\dot{\sigma}, T)$.

$$\begin{aligned} &K^*(t,\dot{a}) \geqslant K_{1a} \Rightarrow K^*(t,\dot{a}) = K_{1D}(\dot{a}) \quad \text{(propagation)}\\ &K^* < K_{1a} \quad \text{(arrest)} \end{aligned} \tag{13}$$

In that framework, the dynamic crack propagation modeling is summing up to the choice of the dynamic crack growth toughness evolution $K_{1D}(\dot{a}, T)$. In practice, this expression is inverted in order to compute the crack growth velocity $\dot{a}$ at each time step. Since no analytical expression of $K_{1D}(\dot{a}, T)$ can be obtained, a large effort has been put in the past to characterize experimentally this parameter. According to the experimental works of Kanninen (1974), Kalthoff and Shockey (1977), Kobayashi et al. (1980), Rosakis (1980), Rosakis and Freund (1982) and Kalthoff (1983), three conditions are required to obtain a physically meaningful law: (i) K_{1D} increases with the crack growth velocity $\dot{a}$; (ii) a critical crack growth velocity exists; and (iii) $\lim_{\dot{a}\to 0} K_{1D}(\dot{a}) \neq K_{1d} \neq K_{1a}$.

From these three conditions, many expressions of the dynamic crack growth toughness evolution have already been proposed. For instance, Kanninen and Popelar (1985) proposed the law (Eq. (14)) and adjusted it on dynamic fracture tests performed by Rosakis and Freund (1982) on DCB 4340 steel specimens (see Fig. 15).

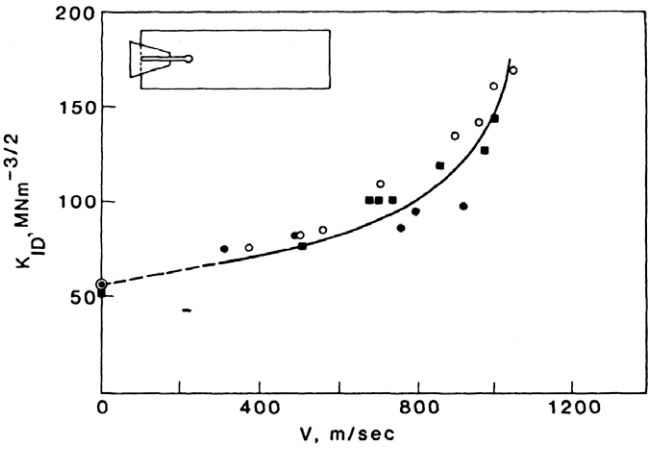

Fig. 15. Dynamic crack growth toughness evolution. Tests performed on (4340 steels) (Rosakis and Freund, 1982) (reproduced from Kanninen and Popelar (1985)).

$$K_{1D}(\dot{a}) = \frac{K_{IA}}{1-\left(\frac{\dot{a}}{V_l}\right)^m} \tag{14}$$

where K_{IA}, V_l and m are material properties which must be evaluated from experiments.

For the numerical simulations of the experimental tests presented in part (2), the dynamic crack growth toughness is assumed given by (15) corresponding to the simpler form of (14) ($m = 1$):

$$K_{1D}(\dot{a}) = \frac{K_{1M}}{1-\frac{\dot{a}}{c_R}} \tag{15}$$

where $K_{1M}(\dot{\sigma}, T)$ is a loading rate and temperature dependent material property which must be evaluated from experiments, $\dot{a}$ the crack tip velocity and c_R is the Rayleigh waves velocity, namely the theoretical maximum velocity of a crack (modes I and II) in a homogeneous medium.

Finally, the dynamic crack propagation criterion is given in Eq. (16) and represented in Fig. 17.

$$\begin{aligned} &K^* < K_{1d} \quad \text{(no initiation)}\\ &K^* = K_{1d}, \quad \theta^* = \theta_c \quad \text{(initiation)}\\ &K^* \geqslant K_{1a} \Rightarrow \dot{a} = c_R\left(1-\frac{K_{1M}}{K^*}\right) \quad \text{(propagation)}\\ &K^* < K_{1a} \quad \text{(arrest)} \end{aligned} \tag{16}$$

where K_{1d} is the dynamic crack initiation toughness, θ_c is the critical direction of propagation, K_{1a} is the dynamic crack arrest toughness.

All the dynamic fracture parameters defined previously depend on the temperature. Though thermoelastic (Rittel, 1998) and thermoplastic (Rittel, 2000) effects have been reported in the literature, the thermodynamic evolution of the system is classically assumed to be isothermal. The experimental fracture tests have been performed at room temperature and the thermo-mechanical phenomena which lead to large temperature variations are not studied here. Therefore, the fracture parameters are assumed to be constant with the temperature.

In the same way, the dynamic fracture parameters are highly dependent on the loading rate and the experimental identification is difficult. If the pre-notch is loaded in mixed-mode loading, the initiation angle can be used to determine the dynamic initiation toughness as shown in Grégoire et al. (2007). If the pre-notch is loaded in pure mode I condition, it is not possible to estimate this parameter directly from the experiments anymore. To determine dynamic fracture parameters vs. loading rate evolution laws, the pure macroscopic modeling is limiting. A micro-scale coupling

can be used to obtain relevant results. These kind of multi-scales approaches are new in dynamic fracture and are not developed here. An alternative solution consists in performing several numerical simulations until convenient values are found. The main issue is that different combinations of the material parameters lead to the same global results. It is hence difficult to determine which combination is physically meaningful. A key for a good choice is a careful comparison between the numerical results obtained with a reliable numerical tool and the well-controlled experimental data. The main advantage of the SHPB setup is that it provides both the input and the output mechanical data (forces and velocities on both sides of the specimen). Therefore, the numerical simulations are performed with the experimental input velocity and, then, the experimental output velocity is used to compare discriminate, and finally validate the numerical results.

3.4. Material properties

Even if the PMMA is known to be viscoelastic, a linear elastic behavior is assumed with a secant dynamic elastic modulus fitted with the velocity of the elastic waves measured during the experiments. Since the experimental tests provided input and output data, the global dynamic Young's modulus is chosen in order to have the correct delay between incident and transmitted signals in the simulations. A secant rather than dynamic Young's modulus is adopted. The material properties used during the numerical simulations of the experimental test presented in Part (2) are collected in Table 3.

3.5. Numerical results

3.5.1. Test 1 (striker velocity: 9.5 m/s)

The mesh is the same for each numerical test and it is shown in Fig. 16. It consists of 1377 four-node elements with four integration points. The numerical calculation of the test 1 requires 120 time steps with a step size chosen as $\Delta t = 5$ μs.

The numerical crack path is shown in Fig. 18. Since the initial notch is machined in such a way that fracture occurs in pure mode I, the crack stays near the specimen symmetry axis all over the propagation as observed during the experiments (Fig. 9).

Fig. 19 shows the comparison between the experimental and numerical crack tip position histories. The dynamic crack propagation criterion equation (16) have been used with $K_{1d} = 1.66\ \mathrm{MPa}\sqrt{\mathrm{m}}$ and $K_{1M} = K_{1a} = 1.22\ \mathrm{MPa}\sqrt{\mathrm{m}}$. As explained by Grégoire et al. (2007), the higher value of K_{1d} has two explanations: firstly, the radius of the initial notch tip is larger than the propagating crack tip radius in the experiments; secondly, the crack initiation point is intrinsically not on the curve characterizing the dynamic crack growth criterion: $\lim_{\dot{a}\to 0} K_{1D}(\dot{a}) \neq K_{1d}$ in Eq. (15) as it has been previously noticed by Ravi-Chandar (2004).

Table 3
Material properties.

Mechanical properties	Symbols (units)	Test 1	Test 2
Density	ρ (kg/m^3)	1190	1190
Static Young's modulus	E_S (GPa)	5.7	5.7
Secant dynamic Young's modulus	E_D^{secant} (GPa)	2.28	2
Poisson's ratio	ν (–)	0.337	0.337
Lamé's constants	λ (GPa)	1.77	1.55
	μ (GPa)	0.85	0.75
Velocity of compressive waves	c_P (m/s)	1708	1599
Velocity of shear waves	c_S (m/s)	847	793
Velocity of one-dimensional elastic waves	c_L (m/s)	1385	1296
Velocity of Rayleigh waves	c_R (m/s)	790	740

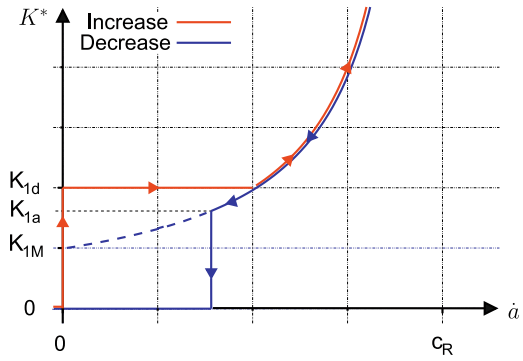

Fig. 16. Dynamic crack propagation criterion.

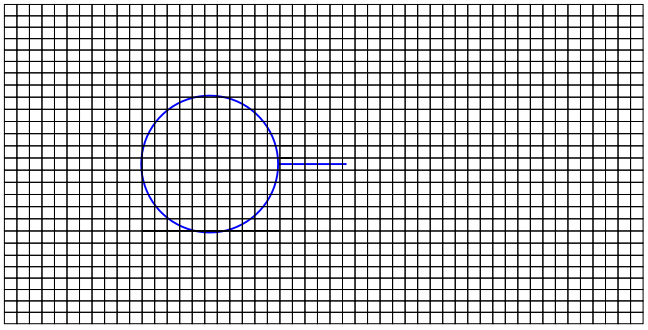

Fig. 17. Mesh and initial notch for the test 1.

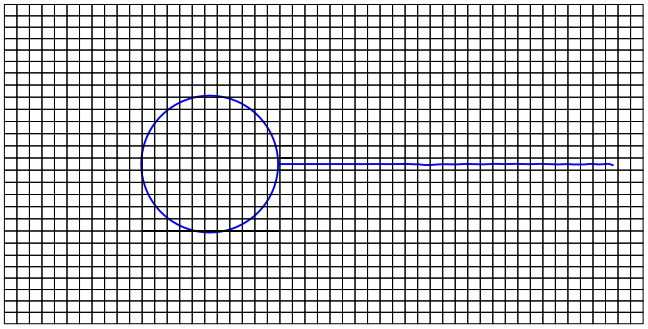

Fig. 18. Mesh and numerical crack path for the test 1.

In Fig. 19, there is a good match of the crack tip position: the crack arrest occurs at the same time and in the same location. Moreover, the crack growth process is well captured since the crack tip velocities are similar during the numerical simulation and the experimental tests.

Fig. 20 shows the comparison between the experimental and numerical velocities histories at the specimen–bar interfaces. Oscillations of the numerical output velocity are noticeable. There are due to numerical noise in the calculations of the velocities and the accelerations after the propagation. Before the initiation, the numerical output velocity match well the experimental output velocity. It is a check of the validity of the numerical impedance model of the output bar.

3.5.2. Test 2 (striker velocity: 7.4 m/s)

The mesh still consists of 1377 four-node elements with four integration points (Fig. 21) but the initial notch is different from the test 1 in order to take into account the first propagation at low striker velocity as explained in Section 2.3.2. The numerical

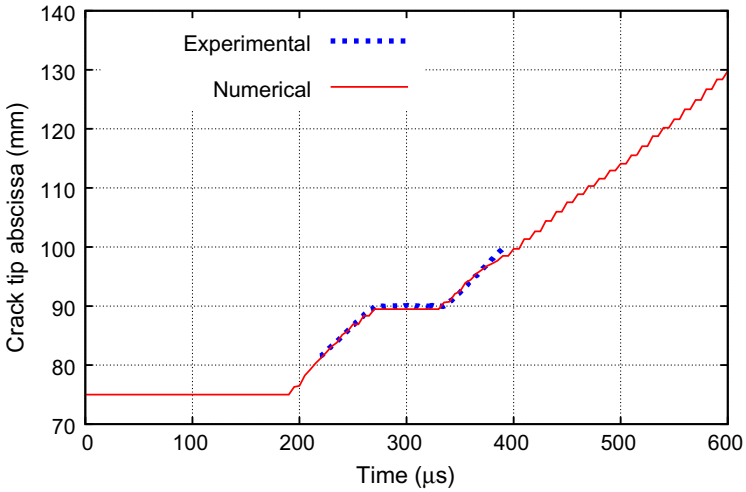

Fig. 19. Comparison of crack tip position histories for the test 1.

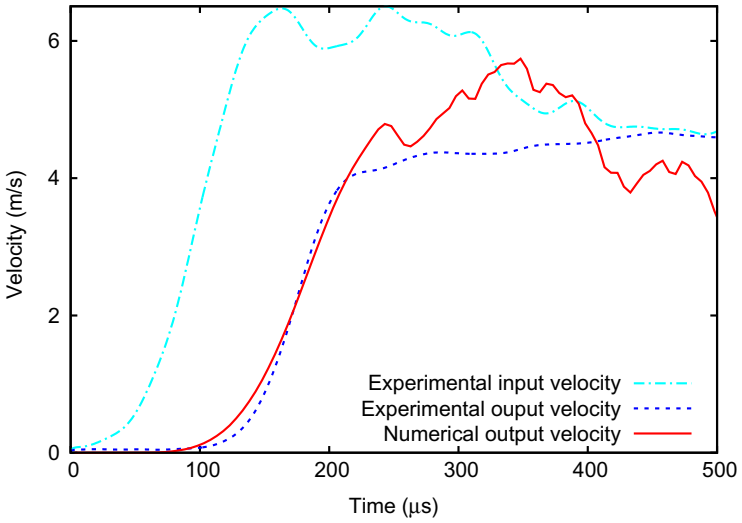

Fig. 20. Comparison of the velocities histories (test 1 – striker velocity: 9.5 m/s).

calculation of the test 2 requires 200 time steps with a step size chosen as $\Delta t = 5$ μs.

The numerical crack path is shown in Fig. 22. The crack still stays near the specimen symmetry axis all over the propagation and the final arrest occurs in the center of the specimen (the crack tip does not reach the specimen border) as observed during the experiments (Fig. 13).

Fig. 23 shows the comparison between the experimental and numerical crack tip position histories. The dynamic crack propagation criterion equation (16) have been used with $K_{1d} = 0.95\ \mathrm{MPa}\sqrt{\mathrm{m}}$ and $K_{1M} = K_{1a} = 0.85\ \mathrm{MPa}\sqrt{\mathrm{m}}$. Since the initial notch radius and the propagating crack tip radius are similar, the value of K_{1d} and K_{1a} are very close. A slight difference remains because the crack initiation point is intrinsically not on the curve

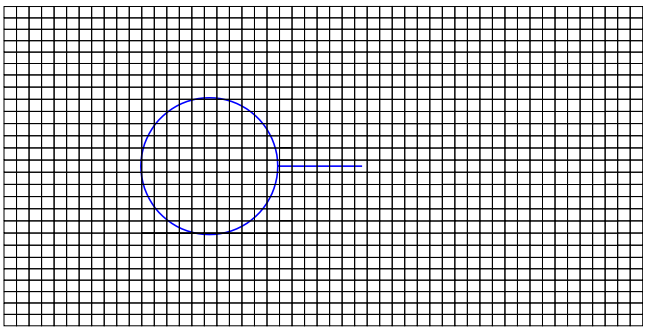

Fig. 21. Mesh and initial notch for the test 2.

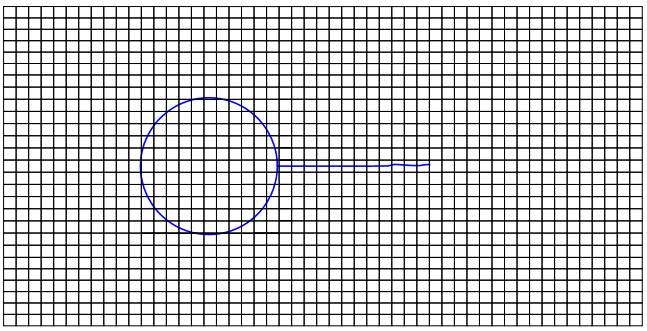

Fig. 22. Mesh and numerical crack path for the test 2.

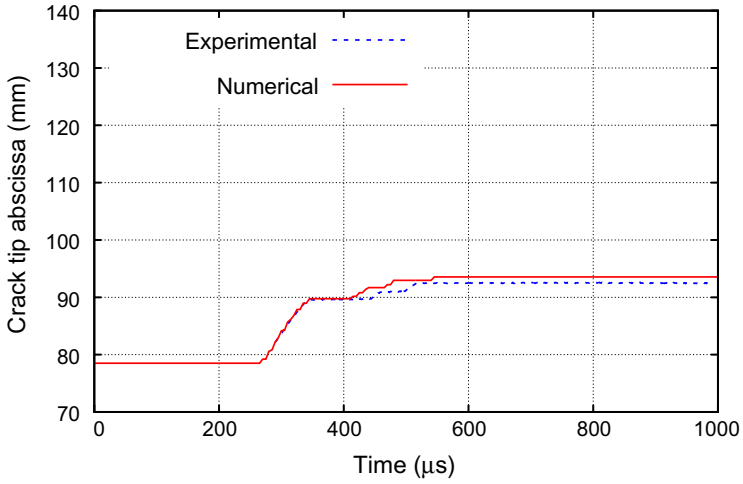

Fig. 23. Comparison of crack tip position histories for the test 2.

characterizing the dynamic crack growth criterion as explained by Ravi-Chandar (2004).

In Fig. 23, there is a good match of the crack position histories and the numerical and experimental first crack arrests occur at the same time and in the same location. The following crack arrests are well located in space but not in time. The criterion (Eq. (16)) is not enough accurate in order to well represent this complex phases similar to the stick-slip phenomenon. By only considering a macroscopic point of view, these results are already satisfying.

4. Conclusion

This work shows that a good combination of well-controlled experiments and refined X-FEM simulations enables one to explain the history of brittle dynamic crack propagation, even during highly transient phases such as crack initiation, crack arrest and crack restart.

The experimental method based on optical displacement sensor provides a highly accurate crack tip position history during a single test. It allows the study of the dynamic phenomena involved during the arrest and the restart of a crack under impact, even for complex propagation cases when the crack path presents several crack arrest and crack restart phases.

The simple ingredients used in the X-FEM modeling seem sufficient to reproduce the phenomena observed during the experiments. The direction of the crack propagation, the different crack arrest and crack restart phases as well as the crack tip velocities are well predict.

Finally, the combination of the experimental and numerical methods developed in this paper gives a good methodology for assessing dynamic crack propagation laws under impact loading for transparent materials. By carrying out extra experimental tests and numerical simulations, the loading rate and temperature dependences of the dynamic crack initiation toughness or the dynamic crack arrest toughness may now be studied.

Acknowledgments

We are grateful to the Laboratoire de Mécanique des Solides, École Polytechnique, France where the experiments were performed. This work was sponsored by the ANR/CNRS Grant DYNRUPT (JC05_45254).

References

Babuska, I., Melenk, J., 1997. The partition of unity method. International Journal for Numerical Methods in Engineering 40, 727–758.
Belytschko, T., Black, T., 1999. Elastic crack growth in finite elements with minimal remeshing. International Journal for Numerical Methods in Engineering 45 (5), 601–620.
Bui, H.D., 1978. Mécanique de la Rupture Fragile. Masson, Paris.
Combescure, A., Gravouil, A., Grégoire, D., Réthoré, J., 2008. X-fem a good candidate for energy conservation in simulation of brittle dynamic crack propagation. Computer Methods in Applied Mechanics and Engineering 197 (5), 309–318.
Dolbow, J., Moës, N., Belytschko, T., 2001. An extended finite element method for modeling crack growth with frictional contact. Computer Methods in Applied Mechanics and Engineering 190 (51), 6825–6846.
Duarte, C., Hamzeh, O., Liszka, T., Tworzydlo, W., 2001. A generalized finite element method for the simulation of three-dimensional dynamic crack propagation. Computer Methods in Applied Mechanics and Engineering 190, 2227–2262.
Erdogan, F., Sih, G., 1963. On the crack extension in plates under plane loading and transverse shear. Journal of Basic Engineering 85, 519–527.
Fineberg, J., Gross, S.P., Marder, M., Swinney, H.L., 1991. Instability in dynamic fracture. Physical Review Letters 67 (4), 457–460.
Freund, L.B., 1990. Dynamic Fracture Mechanics. Cambridge University Press, Cambridge.
Gravouil, A., Moës, N., Belytschko, T., 2002. Non-planar 3D crack growth by the extended finite element and level sets – part ii: level set update. International Journal for Numerical Methods in Engineering 53, 2569–2586.
Grégoire, D., Maigre, H., Réthoré, J., Combescure, A., 2007. Dynamic crack propagation under mixed-mode loading – comparison between experiments and x-fem simulations. International Journal of Solids and Structures 44 (20), 6517–6534.
Irwin, G., 1957. Analysis of stresses and strains near the end of a crack traversing a plate. Journal of Applied Mechanics 24 (3), 361–364.
Kalthoff, J.F., 1983. On some current problems in experimental fracture dynamics. In: Workshop on Dynamic Fracture, pp. 11–35.
Kalthoff, J., Shockey, D., 1977. Instability of cracks under impulse loads. Journal of Applied Physics 48, 986.
Kanninen, M., 1974. A dynamic analysis of unstable crack propagation and arrest in the DCB test specimen. International Journal of Fracture 10 (3), 415–430.
Kanninen, M., Popelar, C.H., 1985. Advanced Fracture Mechanics. Oxford University Press, Oxford.
Karimzada, T., Maigre, H., 2000. Modelisation of dynamic crack propagation criteria. In: Proceedings of the Sixth International Conference on Mechanical and Physical Behaviour of Materials under Dynamic Loading, vol. 10, Krakow, Poland, pp. 461–466.
Kobayashi, A., Seo, K., Jou, J., Urabe, Y., 1980. A dynamic analysis of modified compact-tension specimens using homalite-100 and polycarbonate plates. Experimental Mechanics 20 (3), 73–79.
Kolsky, H., 1949. An investigation of the mechanical properties of material at a very high rate of loading. In: Proceedings of the Physical Society, vol. B 62, pp. 676–700.
Maigre, H., Rittel, D., 1993. Mixed-mode quantification for dynamic fracture initiation: application to the compact compression specimen. International Journal of Solids and Structures 30 (23), 3233–3244.
Menouillard, T., 2007. Dynamique explicite pour la simulation numérique de propagation de fissure par la méthode des éléments finis étendus. Ph.D. Thesis, INSA-LYON.
Moës, N., Belytschko, T., 2002. Extended finite element method for cohesive crack growth. Engineering Fracture Mechanics 69 (7), 813–833.

Moës, N., Dolbow, J., Belytschko, T., 1999. A finite element method for crack growth without remeshing. International Journal for Numerical Methods in Engineering 46, 131–150.

Newmark, N.M., 1959. A method of computation for structural dynamics. Journal of the Engineering Mechanics Division – ASCE 85, 67–94.

Owen, D.M., Zhuang, S., Rosakis, A.J., Ravichandran, G., 1998. Experimental determination of dynamic crack initiation and propagation fracture toughness in thin aluminium sheets. International Journal of Fracture 90, 153–174.

Prabel, B., 2007. Modélisation avec la méthode x-fem de la propagation dynamique et de l'arrt de fissure de clivage dans un acier de cuve rep. Ph.D. Thesis, INSA-LYON.

Ravi-Chandar, K., 2004. Dynamic Fracture. Elsevier, Amsterdam.

Réthoré, J., Gravouil, A., Combescure, A., 2004. A stable numerical scheme for the finite element simulation of dynamic crack propagation with remeshing. Computer Methods in Applied Mechanics and Engineering 193 (42-44), 4493–4510.

Réthoré, J., Gravouil, A., Combescure, A., 2005a. A combined space–time extended finite element method. International Journal for Numerical Methods in Engineering 64, 260–284.

Réthoré, J., Gravouil, A., Combescure, A., 2005b. An energy conserving scheme for dynamic crack growth with the extended finite element method. International Journal for Numerical Methods in Engineering 63, 631–659.

Rittel, D., 1998. Transient temperature measurement using embedded thermocouples. Experimental Mechanics 38 (2), 73–78.

Rittel, D., 2000. A note on the dynamic failure of PMMA. International Journal of Fracture 106 (2), 3–8.

Rittel, D., Maigre, H., 1996. An investigation of dynamic crack initiation in PMMA. Mechanics of Materials 23 (3), 229–239.

Rosakis, A.J., 1980. Analysis of the optical method of caustics for dynamic crack propagation. Engineering Fracture Mechanics 13 (2), 331–347.

Rosakis, A.J., Freund, L.B., 1982. Optical measurement of the plastic strain concentration at a crack tip in a ductile steel plate. Journal of Engineering Materials and Technology 104 (2), 115–120.

Stalder, B., Béguelin, P., Kausch, H.H., 1983. A simple velocity gauge for measuring crack growth. International Journal of Fracture 22 (2), R47–R50.

Zhao, H., Gary, G., 1995. A three dimensional analytical solution of the longitudinal wave propagation in an infinite linear viscoelastic cylindrical bar, application to experimental techniques. Journal of Mechanics and Physics of Solids 43 (8), 1335–1348.